

Anomalous Stark shift of excitonic complexes in monolayer WS₂Nithin Abraham¹,[✉] Kenji Watanabe,² Takashi Taniguchi,³ and Kausik Majumdar^{1,*}¹*Department of Electrical Communication Engineering, Indian Institute of Science, Bangalore 560012, India*²*Research Center for Functional Materials, National Institute for Materials Science, 1-1 Namiki, Tsukuba 305-0044, Japan*³*International Center for Materials Nanoarchitectonics, National Institute for Materials Science, 1-1 Namiki, Tsukuba 305-0044, Japan*

(Received 16 October 2020; revised 18 January 2021; accepted 1 February 2021; published 19 February 2021)

Monolayer transition-metal dichalcogenide (TMDC) semiconductors host strongly bound two-dimensional excitonic complexes, and form an excellent platform for probing many-body physics through manipulation of Coulomb interaction. The quantum confined Stark effect is one of the routes to dynamically tune the emission line of these excitonic complexes. In this paper, using a high-quality graphene/hexagonal boron nitride (hBN)/WS₂/hBN/Au vertical heterojunction, we demonstrate an out-of-plane electric-field driven change in the sign of the Stark shift from blue to red for four different excitonic species, namely, the neutral exciton, the charged exciton (trion), the charged biexciton, and the defect-bound exciton. Such universal nonmonotonic Stark shift with electric field arises from a competition between the conventional quantum confined Stark effect driven redshift and a suppressed binding-energy driven anomalous blueshift of the emission lines, with the latter dominating in the low-field regime. We also find that the encapsulating environment of the monolayer TMDC plays an important role in wave-function spreading, and hence in determining the magnitude of the blue Stark shift. The results for neutral and charged excitonic species are in excellent agreement with calculations from the Bethe-Salpeter equation that use a seven-band per spin tight-binding Hamiltonian. The findings have important implications in probing many-body interaction in two dimensions as well as in developing layered semiconductor based tunable optoelectronic devices.

DOI: [10.1103/PhysRevB.103.075430](https://doi.org/10.1103/PhysRevB.103.075430)**I. INTRODUCTION**

The ability to dynamically tune the absorption and emission properties of strongly luminescent materials is a highly desired trait for realizing tunable optoelectronic devices. The Stark effect [1] is one such phenomenon where an external electric field is used to perturb the electronic structure of the active material and usually provides a redshift in the emission line due to a reduction in the band gap. In the quantum confined Stark effect (QCSE), the electric field is applied along the confinement direction of a quantum well or other nanostructures, thereby allowing a large electric field resulting in a giant shift in the emission line well beyond the binding energy of the exciton without causing field ionization [2–6]. QCSE finds widespread application in ultrafast optical modulators [7–9], self-electro-optic-effect devices [10,11], tunable lasers, and detectors [12,13]. Recent advances in the growth of two-dimensional materials and their atomically thin nature have opened up possibilities to explore the interesting physics of these material systems under high electric fields [14–16]. The monolayer transition-metal dichalcogenides (TMDCs) are a family of atomically thin semiconductors which host strongly bound excitonic complexes, and serve as an excellent test bed for the investigation of QCSE [17–24]. The overall energy shift (ΔE) of the exciton peak due to QCSE has two components. A redshift (ΔE_1) arises due to the opposite movement in energy of the constituent electron state in the conduction

band and the hole state in the valence band, and is given by $\Delta E_1 = -\gamma'F - \gamma''F^2$ where F is the electric field along the out-of-plane direction, and γ' and γ'' are, respectively, the corresponding dipole moment and polarizability. The presence of reflection symmetry in monolayer TMDCs makes the linear term zero, and we only observe a Stark shift that is quadratic with the applied electric field. The other component of the Stark shift, which is a blueshift (ΔE_2), results from a suppression of the exciton binding energy due to the opposite motion of the wave function of the constituent electron and hole within the quantum well under the electric field. For a square well, using second-order perturbation theory, one obtains $\gamma'' \propto t^4$ where t is the quantum well thickness [25]. Thus, in typical quantum wells with width extending up to several nanometers, the quadratic redshift significantly dominates over the blueshift, and thus a blue Stark shift is usually not observed. Monolayer TMDCs, owing to the extremely strong confinement due to their subnanometer thickness, show a relatively weak redshift due to QCSE, and form an interesting platform for possible observation of blue Stark shift.

In this paper we demonstrate a direct observation of conspicuous blue Stark shift and redshift in a clean graphene/hexagonal boron nitride (hBN)/WS₂/hBN/Au heterojunction depending on the magnitude of the electric field applied. Accordingly, the effective shift becomes nonmonotonic with the magnitude of the electric field, with the blueshift dominating at the low-field regime, which can be switched to a net redshift at higher electric field. The results are in excellent agreement with theoretical results obtained by solving the Bethe-Salpeter equation (BSE) that uses a

*kausikm@iisc.ac.in

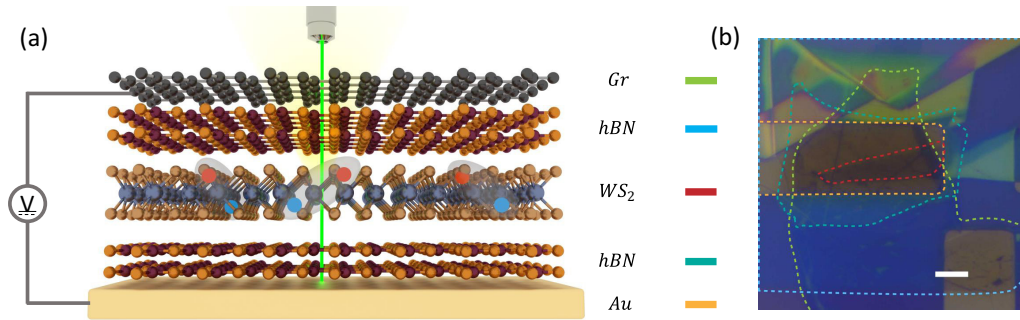


FIG. 1. Device schematic and experimental setup. (a) Schematic representation of the graphene/hBN/WS₂/hBN/Au heterostructure used to investigate the effect of electric field on various multiparticle complexes. Field dependent PL spectra under a 532-nm laser excitation are collected through the transparent top graphene electrode in a back reflection geometry. (b) Optical image delineating various layers of a sample device. Color of the lines map to the bars shown in (a). Scale bar is 5 μm .

seven-band per spin quasiparticle Hamiltonian. Further, a similar tunable shift is demonstrated for other excitonic complexes including charged excitons, charged biexcitons, and defect-bound excitons. Such field tunable Stark redshift and blueshift in different excitonic complexes provides additional Stark tunability that has direct implication in building layered material based tunable optoelectronic devices [26–28].

II. RESULTS AND DISCUSSION

A monolayer of tungsten disulphide (1L-WS₂), which exhibits strong excitonic luminescence at room temperature, is chosen as the active material in this paper. Few-layer hBN flakes are used to encapsulate the WS₂ film and form the top and the bottom dielectric layers. The hBN encapsulated stack is sandwiched between a bottom Au line and a top few-layer graphene film. The Au layer serves the dual role of the bottom electrode and the back reflector while the graphene layer acts as a transparent top electrode, as schematically illustrated in Fig. 1(a). The whole device fabrication has been performed by transferring layers onto prepatterned electrodes, thus avoiding any chemical processing during fabrication, which helps to retain the pristine nature of the flakes and high quality of the interfaces. Details of the device fabrication is provided in the Methods section and the various steps are depicted in Supplemental Material Fig. 1 [29]. Five such samples D1–D5 with varying hBN thickness are fabricated and measured. All samples except D2 are annealed at 70° C for 5 h at a pressure of 10^{−6} Torr. The optical micrograph of a typical device after completion of fabrication is shown in Fig. 1(b). To investigate the effect of an out-of-plane electric field, an electric field is set up between the bottom metal and the top graphene layer. The 1L-WS₂ layer is kept electrically floating to avoid direct carrier injection, and thus avoid any unintentional electrostatic doping effect. The high quality of the hBN layers ensures low gate leakage current in the applied bias range, as shown in Supplemental Material Fig. 2 [29] for all the samples. At each electric field, the stack is excited with a 532-nm laser and the photoluminescence (PL) spectra are collected in a back-reflection geometry. The laser power density is kept below 5 $\mu\text{W}/\mu\text{m}^2$ (50 $\mu\text{W}/\mu\text{m}^2$ for sample D2) to avoid any unintentional heating of the flake.

The symbols in Fig. 2(a) depict the variation in the position of the neutral exciton (X^0) from sample D1 as a function of the applied bias (V_{ext}) at the top electrode with respect to the bottom electrode at 300 K. The electric field seen by the 1L-WS₂ is found out by assuming the continuity of out-of-plane component of the electric displacement vector across the hBN/WS₂/hBN quantum well. The right axis shows the relative shift in X^0 position from $V_{\text{ext}} = 0$ V. To accurately capture the spectral features of the constituent peaks, the experimentally obtained spectra are fitted with Voigt profiles as shown in Supplemental Material Fig. 3 [29]. The Voigt profile, which is a convolution between Lorentzian and Gaussian profiles, accurately captures the homogeneous and inhomogeneous aspects of the individual peaks and fits the PL spectra with good stability. The error from multiple such fits is given as the error bar in Fig. 2(a) and is negligible compared to the observed shifts. The overall shift remains roughly symmetric about $V_{\text{ext}} = 0$ V. The shift in X^0 position initially shows a blueshift with a maximum shift of 1.7 meV occurring at $|V_{\text{ext}}| \approx 2$ V. With $|V_{\text{ext}}| > 2$ V, the feature turns around, with a net redshift appearing at larger $|V_{\text{ext}}|$. To support the repeatability of the observations, results from another sample (D4) are given in Supplemental Material Fig. 4(a) [29] exhibiting a similar trend.

Such a trend contrasts with the previous reports on QCSE in monolayer TMDCs [17,23,30] where the spectral peaks exhibit a parabolic redshift with applied field. To reproduce the observations from the existing literature, we measure the field modulation of the X^0 peak from sample D2, which, similar to the samples from the previous reports, is not vacuum annealed at any point during the fabrication. Measured X^0 peak positions as a function of V_{ext} are given in Fig. 2(b). The data exhibit a parabolic redshift in conformance with the expected second-order Stark shift. The dissimilarity between Figs. 2(a) and 2(b) hints at the importance of the vacuum annealing step for observing the reported anomalous shift which will be discussed later.

For sample D1 in Fig. 2(a), the redshift at higher $|V_{\text{ext}}|$ is expected due to QCSE which results from a reduction in band gap arising from a change in the electronic band structure driven by the out-of-plane electric field [2]. However, the observations at small $|V_{\text{ext}}|$ clearly differ from conventional QCSE. The anomalous blueshift at small $|V_{\text{ext}}|$ is purely an

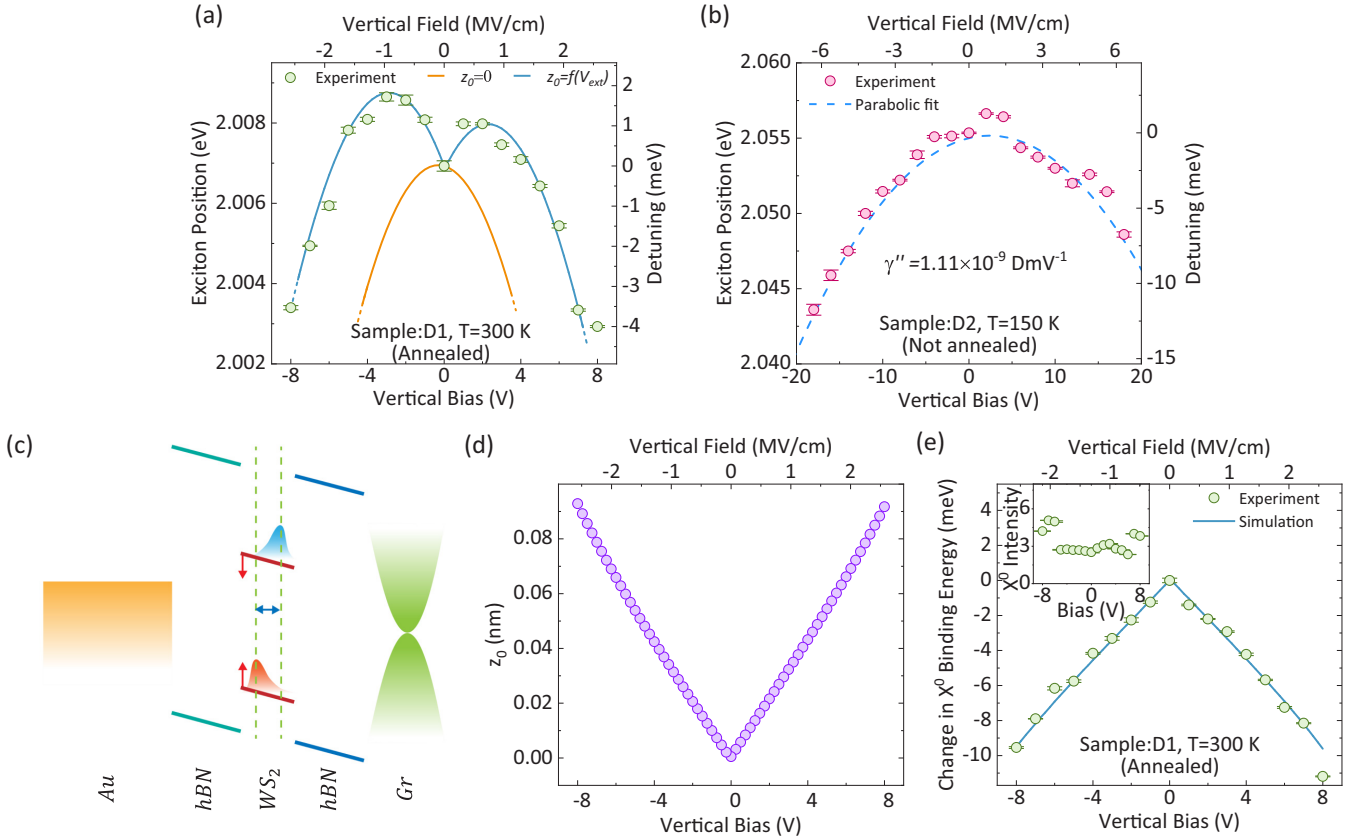


FIG. 2. Field dependence of exciton (X^0) peak. (a) Experimental data on D1 (annealed sample) at 300 K showing blueshift and redshift of the peak at various field regimes along with simulation with (blue trace) and without (orange trace) considering electron-hole separation (z_0) induced binding-energy reduction. Error bars indicate the standard deviation of the X^0 peak position obtained from multiple fits to the measured data. (b) Experimental data from D2 (nonannealed sample) showing absence of blueshift and a strict adherence to a parabolic redshift. A parabolic fit to the data is given by the dashed line. Error bars indicate the standard deviation of the X^0 peak position obtained from multiple fits to the measured data. (c) Schematic band diagram of the device illustrating various effects determining the Stark shift of the exciton. Quasiparticle levels in WS_2 undergo a band-gap reduction (illustrated with red arrows) leading to a redshift in the emission. Wave functions of the interacting quasiparticles experience an out-of-plane separation (marked with blue arrows) leading to a reduction in binding energy and hence a blueshift. (d) Modulation of the separation between electron and hole as a function of applied electric field. (e) Circles (blue trace) depicting expected binding-energy reduction obtained from the difference of measured (simulated) X^0 position and simulation with $z_0 = 0$ showing a linear reduction of binding energy with applied voltage. Error bars represent the standard deviation of the X^0 peak position obtained from multiple fits to the measured data. Inset: Measured PL emission intensity of the X^0 peak as a function of the applied voltage. Error bars indicate the standard deviation of the X^0 peak intensity obtained from multiple fits to the measured data.

excitonic effect and is a consequence of the redistribution of electron and hole quasiparticle wave functions constituting the exciton [2]. The electric field creates an out-of-plane separation between the electron and the hole wave functions, generating a static dipole moment along the out-of-plane direction as schematically illustrated in Fig. 2(c). The extent of this separation is determined by the width and the energy offset provided by the barrier layer. This separation reduces the attractive interaction between the electron and the hole, leading to a reduction in the binding energy of the exciton with an increasing field, which manifests as the observed blueshift.

To obtain physical insights, we first evaluate the electric-field dependent band gap at the $K(K')$ point in monolayer WS_2 using a seven-band per spin tight-binding Hamiltonian [31] where tungsten d orbitals and sulfur p orbitals form the basis. The details of the Hamiltonian are discussed in Supplemental Material Methods S1.1 [29]. Next, in order to

include the excitonic effect, we form the two-particle exciton Hamiltonian and obtain the energy eigenvalues at the zero center-of-mass momentum ($\vec{Q} = \vec{0}$) by solving the BSE [32]. The details of the calculations are provided in Supplemental Material Methods S1.2 [29]. An external bias dependent separation [$z_0(V_{\text{ext}})$] between electron and hole wave functions in the out-of-plane direction modifies the Rytova-Keldysh interaction potential [33,34] in the BSE as [35–37]

$$\tilde{V}_{\vec{q}, V_{\text{ext}}} = \frac{2\pi e^2 e^{-qz_0}}{q} \frac{1}{\epsilon(q)} \quad (1)$$

where, for the case of identical dielectric environment at the top and the bottom of the monolayer,

$$\epsilon(q) = \frac{(1 + pe^{-\eta qd})\kappa}{(1 - pe^{-\eta qd})} + r_0 q e^{-qz_0}. \quad (2)$$

Here, e is the electronic charge; $p = (\epsilon_{\text{env}} - \kappa)/(\epsilon_{\text{env}} + \kappa)$; $\eta = \sqrt{\epsilon_{\parallel}/\epsilon_{\perp}}$; $\kappa = \sqrt{\epsilon_{\parallel}\epsilon_{\perp}}$; d is the thickness of the monolayer; r_0 is a measure of the screening length [38]; $\epsilon_{\text{env}} = \sqrt{\epsilon_{\parallel\text{hBN}}\epsilon_{\perp\text{hBN}}}$ is the dielectric constant of the environment; ϵ_{\parallel} and ϵ_{\perp} are, respectively, the in-plane and out-of-plane dielectric constants of the TMDC; and $\epsilon_{\parallel\text{hBN}}$ and $\epsilon_{\perp\text{hBN}}$ are, respectively, the in-plane and out-of-plane dielectric constants of the hBN. Choices of the dielectric constants [39] are detailed in Supplemental Material Methods S1.2 [29]. The separation $z_0(V_{\text{ext}})$ is estimated for each applied bias as $z_0(V_{\text{ext}}) = |\langle \Psi_e(V_{\text{ext}}) | \hat{z} | \Psi_e(V_{\text{ext}}) \rangle - \langle \Psi_h(V_{\text{ext}}) | \hat{z} | \Psi_h(V_{\text{ext}}) \rangle|$ and is shown in Fig. 2(d). $\Psi_{e/h}(V_{\text{ext}})$ are the electron or hole wave functions in the presence of the applied bias V_{ext} , as obtained from solving the one-dimensional Schrödinger equation along the out-of-plane direction, and \hat{z} is the position operator along the out-of-plane direction of the TMDC. To account for the small asymmetry about $V_{\text{ext}} = 0$ V in the experimental data, air gaps with thickness of few angstroms are added at the top and the bottom interfaces between TMDC and hBN layers in the simulation and are used as a fitting parameter. The orange trace in Fig. 2(a) is obtained by setting $z_0(V_{\text{ext}}) = 0$, which corresponds to the case without any electric-field dependent modification on the interaction potential, and follows a quadratic redshift, as expected. For $z_0(V_{\text{ext}}) \neq 0$, the interaction potential is modified according to Eq. (1) and hence the binding energy of the exciton decreases, leading to the blue trace for the exciton eigenenergies in Fig. 2(a)—in good agreement with the experimental observations.

In order to estimate the out-of-plane polarizability γ'' of the X^0 peak with (D1) and without (D2) the vacuum annealing step, we first calculate the out-of-plane electric field F seen by the TMDC layer as

$$F = \frac{V_{\text{ext}}}{d + d_{\text{hBN}} \frac{\epsilon_{\perp,0,\text{TMD}}}{\epsilon_{\perp,0,\text{hBN}}}} \quad (3)$$

where d_{hBN} is the total thickness of the top and the bottom hBN layers, and $\epsilon_{\perp,0,\text{TMD}} (= 6.3)$ and $\epsilon_{\perp,0,\text{hBN}} (= 3.76)$ are the static out-of-plane dielectric constants of 1L-WS₂ and hBN, respectively [39]. F is shown in the top axes of Figs. 2(a), 2(b), and 2(e), and is less compared to $\frac{V_{\text{ext}}}{d + d_{\text{hBN}}}$ owing to the difference between $\epsilon_{\perp,0,\text{TMD}}$ and $\epsilon_{\perp,0,\text{hBN}}$. A parabolic fit [dashed line in Fig. 2(b)] models the data from D2 accurately and reveals a $\gamma'' = 1.11 \times 10^{-9}$ D m/V [17,23,30]. At the same time, a second-order fit to the experimental data at high electric-field points from D1 results in an estimated effective γ'' of 3.72×10^{-9} D m/V. The clear departure from a parabolic trend for D1 points to the deviation of the experimental data from a second-order relationship expected from a pure quasiparticle effect [1] and hints at the presence of a stronger electric-field induced suppression of exciton binding energy for D1.

The blue Stark shift and the larger value of γ'' in D1 as opposed to D2 are directly linked to the vacuum annealing step employed as well as the choice of materials. Transferred layered heterojunctions inevitably contain unintentional gaps at the interface between them. These gaps originate from air pockets and trapped organic polymer residues from the transfer process, both of which have low dielectric constants. Slow vacuum annealing was proposed to mitigate this effect

[40] and also to achieve a cleaner interface [41]. The interface gap relaxes the net electric field seen by the monolayer TMDC due to the lower dielectric constant of trapped material [see Eq. (3)] and manifests as a reduced polarizability. This effect can be quite significant depending on the thickness of the interface gap. Presence of the gap also introduces a larger energy barrier (compared to hBN) for the quasiparticles in the TMDC. This blocks an easy displacement of the quasiparticle wave functions in the out-of-plane direction, which is essential for the observation of the reported blueshift and to achieve a larger polarizability [42]. The vacuum annealing step either reduces or eliminates the gap, as is the case for D1. Apart from the annealing step, the choice of the combination of the TMDC and the barrier layer is also crucial. hBN provides lower band offsets to 1L-WS₂ compared with gate dielectrics like Al₂O₃ or SiO₂. hBN also provides a superior interface quality as well as a lower gate leakage current density which are critical for reliable observations.

The change in the exciton binding energy with field is obtained in Fig. 2(e) as the deviation of experimental data to the expected parabolic trend obtained by setting $z_0(V_{\text{ext}}) = 0$ in the interaction potential. The blue trace in the same figure shows the difference between blue and orange traces in Fig. 2(a). The linear but small variation of z_0 with V_{ext} shown in Fig. 2(d) suggests strong confinement and that we broadly remain in the QCSE regime over the entire range of applied V_{ext} . This allows conventional QCSE which shows a parabolic nature to dominate at higher-field regimes. This is in good agreement with the experimental observation of photoluminescence intensity being a very weak function of the applied V_{ext} as shown in the inset of Fig. 2(e). This also agrees well with the calculated relative change in the exciton oscillator strength [43] (see Supplemental Material Fig. 7 [29]), which does not vary appreciably in the applied bias range.

To extend the study beyond two particle complexes, we further investigate the effect for higher-order excitonic complexes and the resulting anomalous blueshift. The distribution of the constituent particles of a negatively charged exciton or trion (X^-), with and without an out-of-plane field, is schematically illustrated in Fig. 3(a) along with a depiction of the recombination mechanism for trion in Figs. 3(b) and 3(c). The trion qualitatively exhibits similar Stark shift as the neutral exciton, though the magnitude of the blueshift is larger, ≈ 5.2 meV. Simulation results with (blue trace) and without (orange trace) considering the field dependent modified Coulomb interaction are also shown in Fig. 3(d). Three particle interactions are accounted for by using a modified BSE [44,45], as explained in Supplemental Material Methods S1.3 [29], along with a bias dependent electron-hole interaction as given in Eq. (1). The precision of the simulation for the trion was limited by the prohibitively large matrix sizes needed for trion simulation. Nonetheless, the qualitative agreement with the experimental results verifies a similar origin for the blueshift in the trion as the neutral exciton.

The separation ($\Delta\varepsilon$) between the X^0 and the X^- peaks is the trion dissociation energy, and is given by [46–48]

$$\Delta\varepsilon(V_{\text{ext}}) = \varepsilon_t(V_{\text{ext}}) + \delta\varepsilon_n \quad (4)$$

where ε_t is the binding energy of the trion, and $\delta\varepsilon_n$ is the energy required for the excess electron to move to an empty

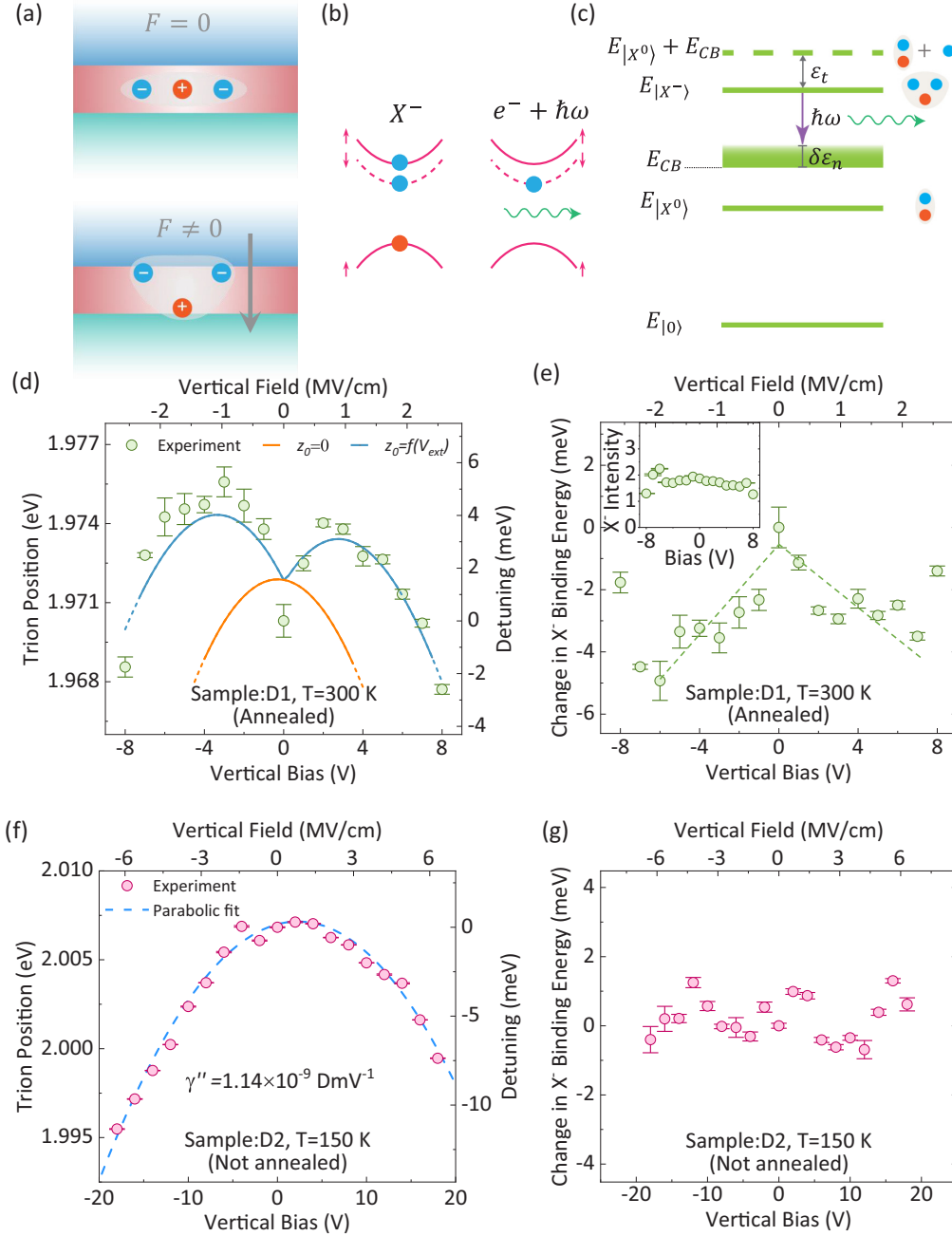


FIG. 3. Field dependence of the trion (X^-) peak. (a) Schematic representation of the orientation of X^- in the absence (top panel) and presence (bottom panel) of an out-of-plane field F . (b) Valley configuration and recombination mechanism for a singlet X^- state in 1L-WS₂. Solid (dashed) lines represent the spin-up (-down) conduction and valence bands. (c) Transition diagram showing radiative decay of X^- . E_{CB} is the lowest conduction-band energy. (d) Experimental peak position of X^- from D1 (annealed sample) at different voltages showing blueshift as well as redshift along with simulation with [$z_0 = f(V_{ext})$, blue trace] and without ($z_0 = 0$, orange trace) considering binding-energy reduction. Error bars indicate the standard deviation of the X^- peak position obtained from multiple fits to the measured data. The dependence of z_0 on V_{ext} and $f(V_{ext})$ is given in Fig. 2(d). (e) Circles (dashed line) representing experimental data (guide to eye) on the modulation of trion binding energy obtained from the separation of X^0 and X^- peaks following Eq. (4). Error bars represent the standard deviation of the trion binding energy obtained from multiple fits to measured data. Inset: Dependence of X^- PL emission intensity on the out-of-plane field. Error bars indicate the standard deviation of the X^- peak intensity obtained from multiple fits to the measured data. (f) Experimental X^- peak position as a function of V_{ext} from D2 (nonannealed sample) exhibiting only redshift. A parabolic fit (dashed line) models the data accurately. Error bars indicate the standard deviation of the X^- peak position obtained from multiple fits to the measured data. (g) Invariance of X^- binding energy with changing V_{ext} for nonannealed sample D2 supporting the absence of blueshift. Error bars represent the standard deviation of the X^- binding energy obtained from multiple fits to the measured data.

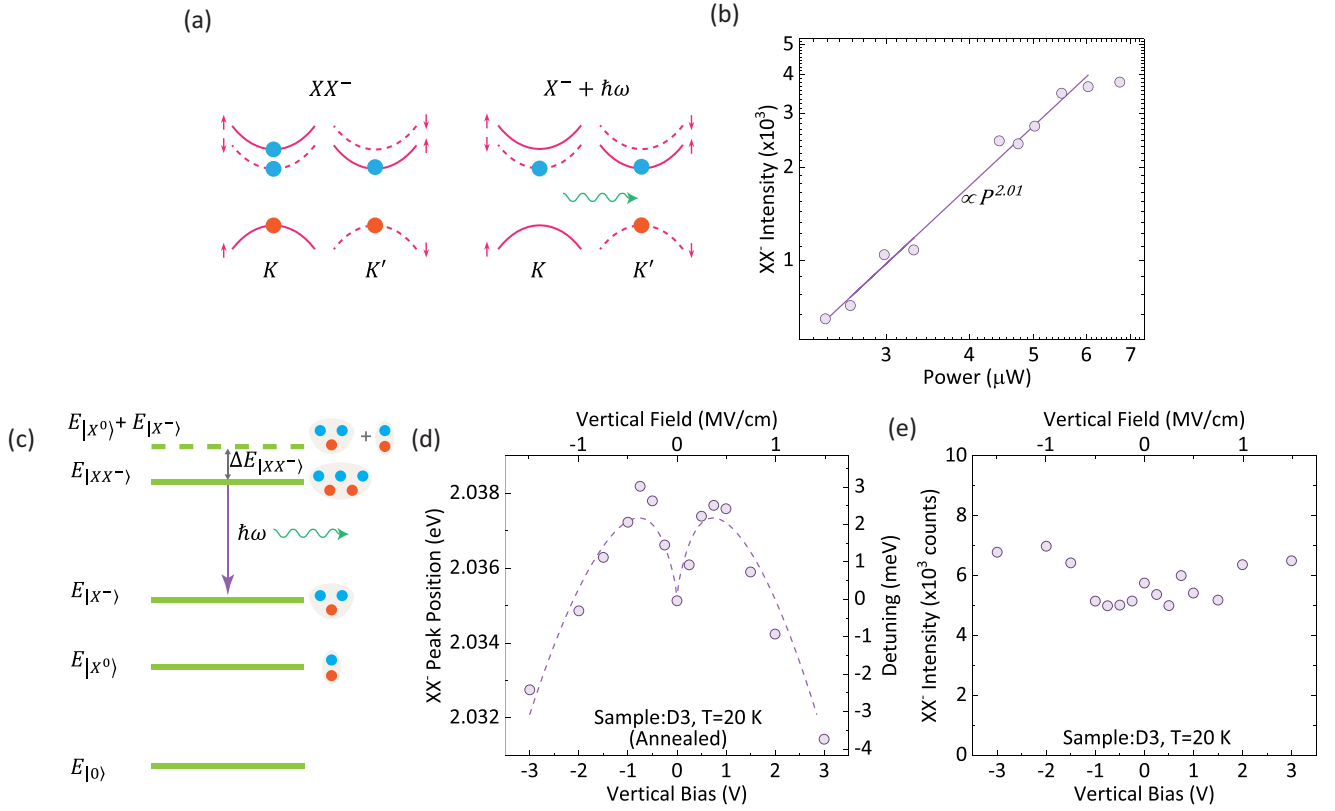


FIG. 4. Field dependence of the charged biexciton (XX^-) peak: (a) Valley configuration of the XX^- state (left) and the remaining dark X^- after photon emission (right). Solid (dashed) lines represent the spin-up (-down) conduction and valence bands. (b) Emission intensity as a function of incident laser power for the charged biexciton peak with a power-law dependence of $\propto P^{2.01}$. (c) Transition diagram showing the radiative decay of XX^- , the states involved in its formation, and the binding energy of XX^- . (d) Field dependent blueshift and redshift for the XX^- peak at 20 K from D3 showing a similar trend as X^0 and X^- along with a guide to the eye (dashed line). (e) XX^- PL emission intensity from D3 being independent of bias.

state in the conduction band. $\delta\varepsilon_n$ is primarily dependent on the doping induced Pauli blocking [49]. In the current structure, where WS_2 remains floating, we do not electrostatically dope the system by the external voltage and thus $\delta\varepsilon_n$ plays the role of an additive constant. The change in $\Delta\varepsilon$ thus provides a direct measure of the reduction in trion binding energy at different V_{ext} . We plot the change in measured $\Delta\varepsilon$ and thereby the modulation of ε_t in Fig. 3(e) as a function of V_{ext} , indicating a strong suppression of the trion binding energy with increasing $|V_{\text{ext}}|$. Note that, similar to the neutral exciton, the trion intensity remains a weak function of V_{ext} [see insets of Figs. 2(e) and 3(e)], suggesting the absence of doping effect in the observations. Similar results from D4 are shown in Supplemental Material Figs. 4(b) and 4(c) [29] indicating the repeatability of our observations. The role of vacuum annealing in observing the blueshift is reiterated by the purely parabolic redshift with $\gamma'' = 1.14 \times 10^{-9}$ D m/V observed for X^- from the nonannealed sample D2 given in Fig. 3(f). The stronger confinement of the electron and the hole wave functions by the interface gap results in negligible change in the trion binding energy induced by the field, which is evident from Fig. 3(g).

A negatively charged biexciton (XX^-) [50,51] is a five-particle excitonic complex consisting of three electrons and two holes. The spin configuration of 1L- WS_2 bands around

the $K(K')$ point forces the lower-energy exciton configuration to be dark. For steady-state measurement, the charged biexciton is formed through a bright (dark) exciton and a dark (bright) trion and has a valley configuration as shown in the left panel of Fig. 4(a). The multiparticle nature of the peak is confirmed by obtaining a quadratic ($\propto P^{2.01}$) variation of PL intensity with applied optical power [Fig. 4(b)]. Note that, when a XX^- emits a photon, the final state is a dark trion [right panel of Fig. 4(a)]. Neglecting the recoil energies, the transition diagram in Fig. 4(c) suggests that the energy of the photon emitted during a XX^- recombination is given by

$$\hbar\omega = E_{|X^0\rangle} - \Delta E_{|XX^-\rangle} \quad (5)$$

where $E_{|X^0\rangle}$ is the neutral exciton emission energy and $\Delta E_{|XX^-\rangle}$ is the XX^- binding energy. The measured Stark shift with $|V_{\text{ext}}|$ for XX^- at 20 K on sample D3 is given in Fig. 4(d) with a maximum blueshift of ≈ 3 meV. The corresponding PL spectra along with the Voigt profile fits are given in Supplemental Material Fig. 8 [29]. Equation (5) suggests that the blueshift for the XX^- peak has two origins: a blueshift in the $E_{|X^0\rangle}$ as explained earlier, and a reduction in $\Delta E_{|XX^-\rangle}$. Along with the anomalous blueshift, like the neutral and charged exciton, we also observe a strong redshift of the XX^- emission peak at higher $|V_{\text{ext}}|$ due to QCSE induced quasiparticle band-gap reduction. The intensity of the XX^-

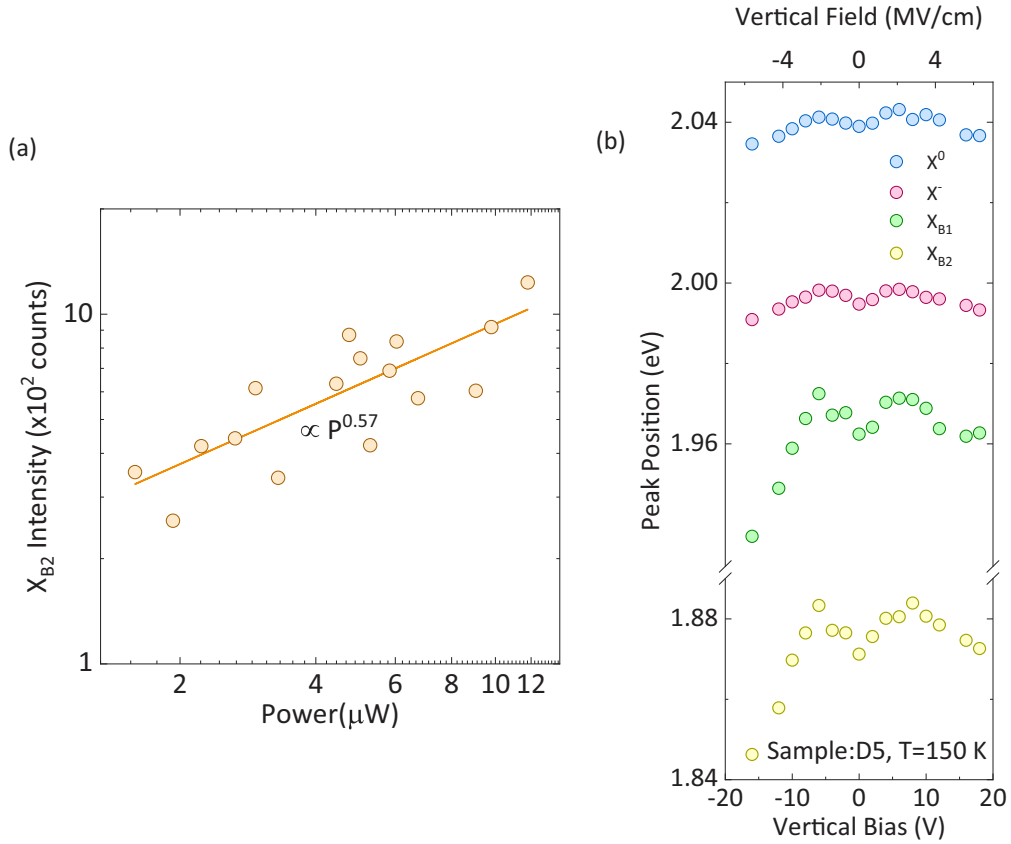


FIG. 5. Verification and field dependence of the defect bound exciton: (a) Variation of the PL intensity of a defect bound excitonic peak as a function of the incident optical power showing a sublinear power dependence. (b) Modulation of the peak positions for different excitonic species as a function of the applied vertical bias from sample D5 at 150 K showing blueshift and redshift at different biasing regimes. Defect bound excitonic peaks X_{B1} and X_{B2} exhibit a larger field modulation compared to the free X^0 and X^- peaks owing to an easily perturbed state of X_{B1} and X_{B2} .

peak as a function of the applied V_{ext} is given in Fig. 4(e). The XX^- intensity being independent of the bias further confirms a constant doping in WS_2 throughout the bias range. A similar trend in the spectral shift of various excitonic complexes points to the universal nature of the phenomenon.

We also probe the electric-field induced peak position shift for a defect bound excitonic complex [52,53]. The defect bound nature of the peak is confirmed by a large inhomogeneous broadening and a sublinear ($\propto P^{0.57}$) variation of PL intensity with incident optical power as shown in Fig. 5(a). Electric-field modulation of the defect bound excitonic peaks X_{B1} and X_{B2} along with the X^0 and X^- peaks is given in Fig. 5(b) and exhibits a similar nonmonotonic Stark shift for both polarities of voltage ranges. The peak positions at each voltage bias are extracted from Voigt profile fits to the experimental data as shown in Supplemental Material Fig. 9 [29]. A relatively large blueshift of ≈ 12.7 meV and an associated giant redshift of ≈ 37.6 meV for peak X_{B2} and a blueshift of ≈ 10.1 meV and a redshift of ≈ 34.9 meV for X_{B1} could be attributed to an easily perturbed state of the defect bound exciton. The universal trend with electric field, though of varying magnitude, in these various multiparticle complexes demonstrates the prevalence of our proposed mechanism in the underlying physics governing these states.

In conventional QCSE structures, current techniques used to obtain blueshift are mainly electrostatic doping [54–56] and relying on the asymmetry of the quantum well structure [57]. Change in doping alters the screening of the charges and in turn modulates the peak position. This can cause a large change in the intensity of the peaks due to transfer of oscillator strength from neutral exciton to charged exciton and vice versa, which is undesirable in many applications as opposed to our observation [Fig. 4(e) and insets of Figs. 2(e) and 3(e)] of intensity being a weak function of the applied bias. Also, in a device with asymmetry, the external field either adds to or cancels the built-in field. Both of these processes are usually asymmetric and depend on the sign of the applied voltage contrary to our observations.

III. CONCLUSIONS

In summary, we demonstrated effective Stark tuning of the emission lines of different excitonic complexes in both red and blue directions through the application of an out-of-plane electric field. The importance of a vacuum annealing step and the suitable choice of materials in reproducing these effects have been emphasized. The ability to control the nature and the magnitude of the Stark shift and the extendibility of the

proposed mechanism to different many-body systems are attractive for layered material based optoelectronic applications, including tunable light emitting diodes, tunable monolayer mirrors, and tuning exciton polaritons through modulation of strong coupling.

IV. METHODS

A. Fabrication

The bottom contact is defined by optical lithography using a 360-nm UV source and AZ5214E resist spin coated on an Si/SiO₂ substrate with 285-nm oxide formed by dry chlorinated thermal oxidation and forming gas annealing. To form the bottom contact, 10-nm Ni and 15-nm Au are sputtered and lifted off by acetone/isopropyl alcohol rinse. The hBN flakes are transferred to a poly-di-methyl-siloxane sheet from Nitto tape. Flakes of suitable thickness are identified by optical contrast and dry transferred to the bottom metal contact. This process is repeated for monolayer WS₂, top hBN, and graphene. Devices except D2 are vacuum annealed in 10⁻⁶-Torr pressure at 70° C for 5 h.

B. Measurements

The devices are wire bonded to a closed cycle He cryostat and connected to a Keithley 4200A-SCS parameter analyzer

for applying an out-of-plane electric field. A 532-nm laser is incident on the sample through a ×50 long working distance objective (numerical aperture = 0.5) and the emitted light is collected in a confocal manner and the spectrum is recorded with a spectrometer with 1800 lines/mm grating and a CCD detector.

Data are available on reasonable request from the corresponding author.

ACKNOWLEDGMENTS

The authors thank Jithin and Prof. Mohan for providing help with the vacuum annealing of the samples, and Veera Pandi for wire bonding of the samples. K.M. acknowledges the support of a grant from the Indian Space Research Organization; a grant from Ministry of Human Resource Development (MHRD) under STARS; Grants under Ramanujan Fellowship and Nano Mission from the Department of Science and Technology (DST), Government of India; and support from MHRD, Ministry of Electronics and Information Technology, and DST Nano Mission through NNetRA. K.W. and T.T. acknowledge support from the Elemental Strategy Initiative conducted by the Ministry of Education, Culture, Sports, Science, and Technology, Japan, Grant No. JPMXP0112101001; Japan Society for the Promotion of Science KAKENHI Grant No. JP20H00354; and JST CREST Grant No. JPMJCR15F3.

-
- [1] J. Stark, Beobachtungen über den Effekt des elektrischen Feldes auf Spektrallinien. I. Quereffekt, *Ann. Phys.* **348**, 965 (1914).
- [2] D. A. B. Miller, D. S. Chemla, T. C. Damen, A. C. Gossard, W. Wiegmann, T. H. Wood, and C. A. Burrus, Band-Edge Electroabsorption in Quantum Well Structures: The Quantum-Confined Stark Effect, *Phys. Rev. Lett.* **53**, 2173 (1984).
- [3] Y. H. Kuo, Y. K. Lee, Y. Ge, S. Ren, J. E. Roth, T. I. Kamins, D. A. Miller, and J. S. Harris, Strong quantum-confined Stark effect in germanium quantum-well structures on silicon, *Nature (London)* **437**, 1334 (2005).
- [4] J. J. Finley, M. Sabathil, P. Vogl, G. Abstreiter, R. Oulton, A. I. Tartakovskii, D. J. Mowbray, M. S. Skolnick, S. L. Liew, A. G. Cullis, and M. Hopkinson, Quantum-confined Stark shifts of charged exciton complexes in quantum dots, *Phys. Rev. B* **70**, 201308(R) (2004).
- [5] A. J. Bennett, R. B. Patel, J. Skiba-Szymanska, C. A. Nicoll, I. Farrer, D. A. Ritchie, and A. J. Shields, Giant Stark effect in the emission of single semiconductor quantum dots, *Appl. Phys. Lett.* **97**, 031104 (2010).
- [6] T. Nakaoka, S. Kako, and Y. Arakawa, Unconventional quantum-confined Stark effect in a single GaN quantum dot, *Phys. Rev. B* **73**, 121305(R) (2006).
- [7] J. E. Roth, O. Fidaner, R. K. Schaevitz, Y.-H. Kuo, T. I. Kamins, J. S. Harris, and D. A. B. Miller, Optical modulator on silicon employing germanium quantum wells, *Opt. Express* **15**, 5851 (2007).
- [8] M. Yamanishi, Ultrafast optical processes in DC-field biased quantum-well structures, *Electron. Comm. Jpn. Pt. II* **75**, 27 (1992).
- [9] Y. H. Kuo, Y. K. Lee, Y. Ge, S. Ren, J. E. Roth, T. I. Kamins, D. A. Miller, and J. S. Harris, Quantum-confined stark effect in Ge/SiGe quantum wells on Si for optical modulators, *IEEE J. Sel. Top. Quantum Electron.* **12**, 1503 (2006).
- [10] H. Haas, P. Gentile, N. Magnea, J. Pautrat, L. S. Dang, and N. Pelekanos, Quantum confined Stark effect (QCSE) and self-electro-optic effect device (SEED) in II-VI heterostructures, in *Semiconductor Materials for Optoelectronics and LTMBE Materials*, European Materials Research Society Symposia Proceedings Vol. 40, edited by J. P. Hirtz, C. Whitehouse, H. P. Meier, H. J. von Bardeleben, and M. O. Manasreh (Elsevier, Amsterdam, 1993), pp. 224–227.
- [11] D. A. B. Miller, Novel optical modulators and bistable devices using the self-electro-optic effect in semiconductor quantum wells, *Surf. Sci.* **174**, 221 (1986).
- [12] P. Steinmann, B. Borchert, and B. Stegmüller, Asymmetric quantum wells with enhanced QCSE: Modulation behaviour and application for integrated laser/modulator, *IEEE Photonics Technol. Lett.* **9**, 191 (1997).
- [13] P. Chaisakul, D. Marris-Morini, G. Isella, D. Chrastina, M. S. Rouified, X. Le Roux, S. Edmond, E. Cassan, J. R. Coudeville, and L. Vivien, 10-Gb/s Ge/SiGe multiple quantum-well waveguide photodetector, *IEEE Photonics Technol. Lett.* **23**, 1430 (2011).
- [14] Y. Chen, Y. Huang, W. Lou, Y. Cai, and K. Chang, Electric-field-driven exciton vortices in transition metal dichalcogenide monolayers, *Phys. Rev. B* **102**, 165413 (2020).

- [15] Z. Jiang, W. Lou, Y. Liu, Y. Li, H. Song, K. Chang, W. Duan, and S. Zhang, Spin-Triplet Excitonic Insulator: The Case of Semihydrogenated Graphene, *Phys. Rev. Lett.* **124**, 166401 (2020).
- [16] Y. Chen, D. Zhang, and K. Chang, Exciton vortices in two-dimensional hybrid perovskite monolayers, *Chinese Phys. Lett.* **37**, 117102 (2020).
- [17] J. Klein, J. Wierzbowski, A. Regler, J. Becker, F. Heimbach, K. Müller, M. Kaniber, and J. J. Finley, Stark effect spectroscopy of mono- and few-Layer MoS₂, *Nano Lett.* **16**, 1554 (2016).
- [18] Z. Wang, Y. H. Chiu, K. Honz, K. F. Mak, and J. Shan, Electrical tuning of interlayer exciton gases in WSe₂ bilayers, *Nano Lett.* **18**, 137 (2018).
- [19] C. Chakraborty, A. Mukherjee, L. Qiu, and A. N. Vamivakas, Electrically tunable valley polarization and valley coherence in monolayer WSe₂ embedded in a van der Waals heterostructure, *Opt. Mater. Express* **9**, 1479 (2019).
- [20] N. Nikolay, N. Mendelson, N. Sadzak, F. Böhm, T. T. Tran, B. Sontheimer, I. Aharonovich, and O. Benson, Very Large and Reversible Stark-Shift Tuning of Single Emitters in Layered Hexagonal Boron Nitride, *Phys. Rev. Appl.* **11**, 041001(R) (2019).
- [21] M. Massicotte, F. Vialla, P. Schmidt, M. B. Lundeberg, S. Latini, S. Hastrup, M. Danovich, D. Davydovskaya, K. Watanabe, T. Taniguchi, V. I. Fal'ko, K. S. Thygesen, T. G. Pedersen, and F. H. Koppens, Dissociation of two-dimensional excitons in monolayer WSe₂, *Nat. Commun.* **9**, 1633 (2018).
- [22] C. Chakraborty, K. M. Goodfellow, S. Dhara, A. Yoshimura, V. Meunier, and A. N. Vamivakas, Quantum-confined Stark effect of individual defects in a van der Waals heterostructure, *Nano Lett.* **17**, 2253 (2017).
- [23] J. G. Roch, N. Leisgang, G. Froehlicher, P. Makk, K. Watanabe, T. Taniguchi, C. Schönenberger, and R. J. Warburton, Quantum-confined Stark effect in a MoS₂ monolayer van der Waals heterostructure, *Nano Lett.* **18**, 1070 (2018).
- [24] J. Pu, K. Matsuki, L. Chu, Y. Kobayashi, S. Sasaki, Y. Miyata, G. Eda, and T. Takenobu, Exciton polarization and renormalization effect for optical modulation in monolayer semiconductors, *ACS Nano* **13**, 9218 (2019).
- [25] J. Singh, *Electronic and Optoelectronic Properties of Semiconductor Structures* (Cambridge University, Cambridge, England, 2003).
- [26] J. Gu, B. Chakraborty, M. Khatoniar, and V. M. Menon, A room-temperature polariton light-emitting diode based on monolayer WS₂, *Nat. Nanotechnol.* **14**, 1024 (2019).
- [27] G. Scuri, Y. Zhou, A. A. High, D. S. Wild, C. Shu, K. De Greve, L. A. Jauregui, T. Taniguchi, K. Watanabe, P. Kim, M. D. Lukin, and H. Park, Large Excitonic Reflectivity of Monolayer MoSe₂ Encapsulated in Hexagonal Boron Nitride, *Phys. Rev. Lett.* **120**, 037402 (2018).
- [28] Y. Zhou, G. Scuri, J. Sung, R. J. Gelly, D. S. Wild, K. De Greve, A. Y. Joe, T. Taniguchi, K. Watanabe, P. Kim, M. D. Lukin, and H. Park, Controlling Excitons in an Atomically Thin Membrane with a Mirror, *Phys. Rev. Lett.* **124**, 027401 (2020).
- [29] See Supplemental Material at <http://link.aps.org/supplemental/10.1103/PhysRevB.103.075430> for details of band-structure calculation, details of BSE calculation for excitons and trions, fabrication steps, leakage current data, results showing repeatability of observations, and raw spectra.
- [30] I. Verzhbitskiy, D. Vella, K. Watanabe, T. Taniguchi, and G. Eda, Suppressed out-of-plane polarizability of free excitons in monolayer WSe₂, *ACS Nano* **13**, 3218 (2019).
- [31] H. Rostami, A. G. Moghaddam, and R. Asgari, Effective lattice Hamiltonian for monolayer MoS₂: Tailoring electronic structure with perpendicular electric and magnetic fields, *Phys. Rev. B* **88**, 085440 (2013).
- [32] F. Wu, F. Qu, and A. H. MacDonald, Exciton band structure of monolayer MoS₂, *Phys. Rev. B* **91**, 075310 (2015).
- [33] N. S. Rytova, The screened potential of a point charge in a thin film, *Moscow Univ. Phys. Bull.* **3**, 18 (1967).
- [34] L. Keldysh, Coulomb interaction in thin semiconductor and semimetal films, *Sov. J. Exp. Theor. Phys. Lett.* **29**, 658 (1979).
- [35] D. Van Tuan, M. Yang, and H. Dery, Coulomb interaction in monolayer transition-metal dichalcogenides, *Phys. Rev. B* **98**, 125308 (2018).
- [36] L. Meckbach, T. Stroucken, and S. W. Koch, Influence of the effective layer thickness on the ground-state and excitonic properties of transition-metal dichalcogenide systems, *Phys. Rev. B* **97**, 035425 (2018).
- [37] L. S. R. Cavalcante, A. Chaves, B. Van Duppen, F. M. Peeters, and D. R. Reichman, Electrostatics of electron-hole interactions in van der Waals heterostructures, *Phys. Rev. B* **97**, 125427 (2018).
- [38] C. Zhang, H. Wang, W. Chan, C. Manolatou, and F. Rana, Absorption of light by excitons and trions in monolayers of metal dichalcogenide MoS₂: Experiments and theory, *Phys. Rev. B* **89**, 205436 (2014).
- [39] A. Laturia, M. L. Van de Put, and W. G. Vandenberghe, Dielectric properties of hexagonal boron nitride and transition metal dichalcogenides: From monolayer to bulk, *npj 2D Mater. Appl.* **2**, 6 (2018).
- [40] S. Tongay, W. Fan, J. Kang, J. Park, U. Koldemir, J. Suh, D. S. Narang, K. Liu, J. Ji, J. Li, R. Sinclair, and J. Wu, Tuning interlayer coupling in large-area heterostructures with CVD-grown MoS₂ and WS₂ monolayers, *Nano Lett.* **14**, 3185 (2014).
- [41] C. Zhang, A. Johnson, C. L. Hsu, L. J. Li, and C. K. Shih, Direct imaging of band profile in single layer MoS₂ on graphite: Quasiparticle energy gap, metallic edge states, and edge band bending, *Nano Lett.* **14**, 2443 (2014).
- [42] M. A. Maize, M. A. Antonacci, and F. Marsiglio, The static electric polarizability of a particle bound by a finite potential well, *Am. J. Phys.* **79**, 222 (2011).
- [43] G. Gupta and K. Majumdar, Fundamental exciton linewidth broadening in monolayer transition metal dichalcogenides, *Phys. Rev. B* **99**, 085412 (2019).
- [44] R. Tempelaar and T. C. Berkelbach, Many-body simulation of two-dimensional electronic spectroscopy of excitons and trions in monolayer transition metal dichalcogenides, *Nat. Commun.* **10**, 3419 (2019).
- [45] M. Drüppel, T. Deilmann, P. Krüger, and M. Rohlfing, Diversity of trion states and substrate effects in the optical properties of an MoS₂ monolayer, *Nat. Commun.* **8**, 2117 (2017).
- [46] K. F. Mak, K. He, C. Lee, G. H. Lee, J. Hone, T. F. Heinz, and J. Shan, Tightly bound trions in monolayer MoS₂, *Nat. Mater.* **12**, 207 (2013).
- [47] B. Stébé and A. Aïné, Ground state energy and optical absorption of excitonic trions in two dimensional semiconductors, *Superlattices Microstruct.* **5**, 545 (1989).

- [48] V. Huard, R. T. Cox, K. Saminadayar, A. Arnoult, and S. Tatarenko, Bound States in Optical Absorption of Semiconductor Quantum Wells Containing a Two-Dimensional Electron Gas, *Phys. Rev. Lett.* **84**, 187 (2000).
- [49] S. Kallatt, S. Das, S. Chatterjee, and K. Majumdar, Interlayer charge transport controlled by exciton-trion coherent coupling, *npj 2D Mater. Appl.* **3**, 15 (2019).
- [50] M. Barbone, A. R. Montblanch, D. M. Kara, C. Palacios-Berraquero, A. R. Cadore, D. De Fazio, B. Pingault, E. Mostaani, H. Li, B. Chen, K. Watanabe, T. Taniguchi, S. Tongay, G. Wang, A. C. Ferrari, and M. Atatüre, Charge-tuneable biexciton complexes in monolayer WSe₂, *Nat. Commun.* **9**, 3721 (2018).
- [51] M. Paur, A. J. Molina-Mendoza, R. Bratschitsch, K. Watanabe, T. Taniguchi, and T. Mueller, Electroluminescence from multi-particle exciton complexes in transition metal dichalcogenide semiconductors, *Nat. Commun.* **10**, 1709 (2019).
- [52] P. K. Chow, R. B. Jacobs-Gedrim, J. Gao, T. M. Lu, B. Yu, H. Terrones, and N. Koratkar, Defect-induced photoluminescence in monolayer semiconducting transition metal dichalcogenides, *ACS Nano* **9**, 1520 (2015).
- [53] S. Tongay, J. Suh, C. Ataca, W. Fan, A. Luce, J. S. Kang, J. Liu, C. Ko, R. Raghunathanan, J. Zhou, F. Ogletree, J. Li, J. C. Grossman, and J. Wu, Defects activated photoluminescence in two-dimensional semiconductors: Interplay between bound, charged, and free excitons, *Sci. Rep.* **3**, 2657 (2013).
- [54] S. Yasukochi, T. Murai, S. Moritsubo, T. Shimada, S. Chiashi, S. Maruyama, and Y. K. Kato, Gate-induced blueshift and quenching of photoluminescence in suspended single-walled carbon nanotubes, *Phys. Rev. B* **84**, 121409(R) (2011).
- [55] A. Chernikov, A. M. van der Zande, H. M. Hill, A. F. Rigosi, A. Velauthapillai, J. Hone, and T. F. Heinz, Electrical Tuning of Exciton Binding Energies in Monolayer WS₂, *Phys. Rev. Lett.* **115**, 126802 (2015).
- [56] X. He, Z. Zhang, C. Zhang, Y. Yang, M. Hu, W. Ge, and X. Zhang, Exploration of exciton behavior in atomically thin WS₂ layers by ionic gating, *Appl. Phys. Lett.* **113**, 013104 (2018).
- [57] R. K. Gug and W. E. Hagston, Large blue shifts induced by the quantum confined stark effect in asymmetric quantum wells, *Appl. Phys. Lett.* **73**, 1547 (1998).